RSC Advances

PAPER

View Article Online
View Journal | View Issue



Cite this: *RSC Adv.*, 2017, **7**, 7392

# Synergistical enhancement of the electrochemical properties of lignin-based activated carbon using $NH_3 \cdot H_2O$ dielectric barrier discharge plasma

Weimin Chen, Xiaoyan Zhou,* Shukai Shi, Nguyen Thiphuong and Minzhi Chen

Received 29th October 2016
Accepted 9th January 2017

DOI: 10.1039/c6ra26010a

www.rsc.org/advances

$NH_3 \cdot H_2O$ dielectric barrier discharge (DBD) plasma was applied in lignin-based activated carbon (LCA) to enhance its electrochemical properties. X-ray photoelectron spectroscopy (XPS), electron spin resonance spectrometry (ESR), automated surface area and pore size analysis, X-ray diffraction (XRD) and Raman spectroscopy (Raman) were performed on LCA and LCANH (LCA treated by $NH_3 \cdot H_2O$ DBD plasma) in order to reveal the changes in physical and chemical structures. An electrochemical workstation was used to investigate the electrochemical properties of LCA and LCANH. The results showed that both nitrogen-containing and oxygen-containing chemical groups were incorporated into the carbon surface after plasma treatment. In addition, the specific surface area and micropores volume of LCANH were 21.7% and 8.5% higher than that of LCA. These facts synergistically enhance the electrochemical properties of activated carbon, allowing it to demonstrate a specific capacitance of 271.7 F $g^{-1}$ for LCANH at a current density of 5 A $g^{-1}$, which are 74.2% higher compared to LCA.



## 1. Introduction

Lignin is the second most abundant natural polymer after cellulose, and its massive annual worldwide yield is around 50 million metric tonnes. Lignin is also the main byproduct from the paper industry and is usually considered as an energy source with low added value.[1] Only a small fraction of lignin is utilized by traditional management, such as burning as a low-valued fuel. In recent years, biomass-based activated carbons with a well-developed porous structure and high specific surface have been widely applied in electrode materials for supercapacitors due to their exceptional advantages of low cost, good physical and chemical stability and high electrical conductivity over carbon nanotubes, carbon nanofibres and graphene sheets.[2–7] Their features of a high carbon content, low-cost, abundance and aromatic nature make lignin attractive as a precursor for the production of activated carbon (AC).

Various treatments, including gas oxidation, supercritical fluids, electrochemical oxidation, ion or cluster bombardment and plasma treatment, are applied in AC surface modification.[8] It is well known that the porous structure and the type, content and bonding mode of heteroatoms (oxygen, sulphur, nitrogen and boron) on the AC surface are the main factors determining its attractive properties.[2,9] Previous studies have found that nitrogen-enriched carbons have excellent adsorption properties for the removal of sulphur(VI) oxide, hydrogen sulphide, nitrogen(II) oxide, carbon(IV) oxide and pollutants from the gas or liquid phase.[10–12] The nitrogen-enriched carbons can be also successfully used in supercapacitor preparation due to its good electrochemical properties.[13,14] Oxygen-containing and nitrogen-containing groups can be introduced into the AC surface by impregnating the precursors or preliminary activated carbon with nitric acid, ammonia or urea solutions in elevated temperatures.[15,16] In particular, the solvent-free, well-controlled, simple operation procedure, its non-pollution nature and short processing time make plasma treatment a promising modification technique. Moreover, plasma treatment can allow simply altering the feed gas ($NH_3$, $O_2$, air, $CO_2$ and $N_2$) for producing different chemically active species on the AC surface without changing the material's bulk properties significantly.[8,17,18]

Previous studies demonstrated that both oxygen-containing and nitrogen-containing groups could be successfully introduced into the surface of viscose-based activated carbon fibres using $NH_3$ dielectric barrier discharge (DBD) plasma, which also leads to a decrease in surface area and pore volume.[19] $O_2$ DBD plasma was also applied in granular activated carbon for enhancing the adsorbability, which was mainly attributed to the change in the surface chemical structure rather than modification of the physical structure.[20] $N_2$ also served as a feed gas used in producing viscose-based activated carbon fibres to support adsorption enhancement.[8] Moreover, oxygen plasma was directly used to activate biomass-derived bio-char.[21] The porous structure of bio-char treated by plasma was improved and oxygen-containing groups were successfully introduced, which resulted in the enhancement of capacitance by 72.3% compared to that achieved by treatment by KOH chemical

*College of Materials Science and Engineering, Nanjing Forestry University, No. 159 Longpan Road, Nanjing 210037, China. E-mail: zhouxiaoyan@njfu.edu.cn; Fax: +86 25 8542 8517; Tel: +86 25 8542 8506*

activation.[21] In addition, our previous study showed that $H_2O$ DBD plasma treatment leads to the successful incorporation of oxygen-containing groups on a wheat straw surface.[22] In this paper, $NH_3 \cdot H_2O$ DBD plasma was applied in lignin-based activated carbon (LCA) for the enhancement of its electrochemical properties. One would expect that DBD plasma would break up the $NH_3 \cdot H_2O$ to obtain radicals and ions like NH, N, OH, *etc.*

In the present study, the electrochemical properties of lignin-based activated carbon modified by $NH_3 \cdot H_2O$ DBD plasma treatment were investigated. Moreover, various characterization methods were applied to reveal the change in physical and chemical structures of LCA before and after plasma treatment. Positive synergistic effects by $NH_3 \cdot H_2O$ DBD plasma treatment on the electrochemical properties are also discussed herein. Such understanding is essential for the utilization of industrial wastes with improved value and for the development of lignin applications in carbon production.

## 2. Material and methods

### 2.1 Preparation of lignin-based activated carbon

Lignin used in this study was extracted from pulping black liquor, which was purchased from a local paper mill (Yonghong, Nanjing, China). The separation and purification process for lignin was presented as follows: distilled water was used to dilute the pulping black liquor with the volume ratio of 1 : 1. Then, 20 wt% $H_2SO_4$ was added into this mixture in order to regulate the pH value to 8.5. This mixture was stirred and heated by a water bath (60 °C) for 4 h. Then, the mixture was subjected to filtration in order to separate the impurities. Distilled water was mixed with the obtained filter liquor with the volume ratio of 5 : 2. Then, 10 wt% HCl was used to regulate the pH value of this system to approximately 2. The mixture was stirred constantly under a temperature of 90 °C for 8 h and aged for 12 h at room temperature to facilitate the polymerization of lignin. Then, the precipitate of lignin was obtained by adding hydrochloric acid and by a subsequent centrifugation until the supernatant was neutral.[23] The obtained lignin was ground and sieved into a particle size (<1 mm), then dried at 103 °C for 4 h.

The carbonization for dried lignin was carried out in a tube furnace (OTF-1200X, China) at 500 °C for 60 min under a 20 mL $min^{-1}$ $N_2$ flow and at a heating rate of 5 °C·$min^{-1}$. The carbonated lignin was added into KOH aqueous solution with the mixing weight ratio (carbonated lignin to KOH) of 1 : 3. The mixture was stirred for 30 min and then dried at 103 °C for 6 h. The dried mixture was then subjected to chemical activation in a tube furnace at 800 °C for 120 min with the same $N_2$ flow and heating rate. After cooling down to room temperature, the obtained product was washed with 1 M HCL and then washed with ultra-pure water several times until the pH reached 7. Finally, the lignin-based activated carbon was dried at 103 °C.

### 2.2 DBD plasma modification

The schematic diagram of the experimental set-up for the DBD plasma treatment is presented in Fig. 1. The DBD plasma reactor (CTP-2000K, China) consisted of a circular parallel-plate with a diameter of 50 mm, a barrier thickness of 3.0 mm and a distance between the barriers of 5.0 mm. Tempered glass and stainless steel were used for the barrier materials and electrodes, respectively. Approximately 1 g of active carbon samples were placed in the reactor chamber for each experiment. The $NH_3 \cdot H_2O$ solution was heated to 75 °C using a water bath and the pressure of the reactor chamber was retained at 20 KPa using a vacuum pump. A large number of reactive species, such as atoms and ions from $NH_3 \cdot H_2O$, were excited in the DBD reactor by applying an AC power with an audio-frequency of 10 kHz and a peak voltage of 5 kV. A series of preliminary experiments were carried out and only the experimental conditions (discharge power, 40 W; reactor chamber pressure, 20 KPa, treating time, 2 min) that could help achieve the highest capacitance are specially presented in this study.

### 2.3 Characterization of activated carbon

X-ray photoelectron spectroscopy (XPS, AXIS Ultra DLD, Japan) was applied to reveal the surface atomic compositions and chemical functional groups of the carbon samples. The survey scanning mode was carried out for low-resolution spectra in the binding energy region of 0–1100 eV. The scanning mode of C 1s (277–396 eV), N 1s (390–410 eV) and O 1s (524–540 eV) for high-resolution spectra were performed with a pass energy of 10 eV and non-monochromatic Mg Kα and Al Kα X-radiation ($h\gamma$ = 1253.7 eV and 1486.7 eV, respectively). The C 1s, N 1s and O 1s spectra were deconvoluted into several components using XPSPEAK Software (version 4.1).

The *g* factor and free radicals concentration of the carbon samples were determined by electron spin resonance spectrometry (ESR, Bruker EMX-10/12, Germany), operated under a microwave frequency of 9.8617 GHz, with a scan time period of 5 min and a time constant of 0.25 s.

Automated surface area and pore size analysis (ASAP 2020, America) was used to record the nitrogen adsorption–desorption isotherms at 77 K. The specific surface area of the carbon samples was calculated by the Brunauer–Emmett–Teller (BET) method. The Barrett–Joyner–Halenda (BJH) method was applied to reveal the pores distribution. The *t*-plot method was used for calculating the micropores volume. The amount adsorbed at a relative pressure of $P/P_0 = 0.99$ was used to estimate the total pore volume. Prior to each experiment, all the carbon samples were subjected to a degassing process at 300 °C for 6 h.

X-ray diffractometry (XRD, Ultima-IV, Japan) was used to investigate the crystalline structure of the carbon samples. The Cu Kα radiation (X-ray wavelength, 0.15406 nm) was applied for recording the diffraction angles in the region of 5–65° at a speed of 0.02° $s^{-1}$. The interlayer spacings of $d_{002}$ and $d_{001}$ were calculated using Bragg's equation, as shown in eqn (1):

$$d = \lambda(2 \sin \theta)^{-1} \quad (1)$$

where $\lambda$ is the X-ray wavelength and $\theta$ is the scattering angle of the diffraction peak.

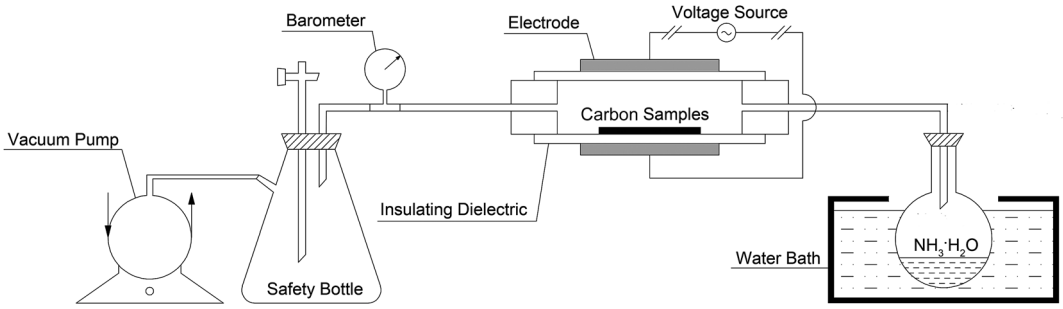


Fig. 1 Schematic diagram of the experimental set-up for the DBD plasma treatment.

Scherrer's equation was used to determine the crystallite size along the *c*-axis ($L_c$) and the size of the layer planes ($L_a$), as presented in eqn (2):

$$L = k\lambda(\beta \cos \theta)^{-1} \quad (2)$$

where $k$ is the shape factor and $\beta$ is the half-width of the diffraction peak, determined by JADE software (version 5.0).

Raman spectroscopy (DXR532, America) was applied to study the aromatic and amorphous structures of the carbon samples. Laser radiation was operated at a wavelength of 532 nm, a spectral resolution of 4 $cm^{-1}$, laser power of 10%, exposure time of 10 s and for a total of 30 acquisitions. The Raman spectra were recorded between the wavenumber region of 800–1800 $cm^{-1}$ and fitted into several Gaussian bands using XPSPEAK Software (Version 4.1).

### 2.4 Preparation and electrochemical measurements of the electrode

Carbon samples, acetylene black and conducting graphite were mixed with the weight ratio of 80 : 10 : 10 in an agate mortar to obtain a homogeneous black powder. Then, 5 wt% of poly(-tetrafluoroethylene) as the binder and a few drops of ethanol were added into this mixture until the carbon slurry was obtained. After briefly evaporating off the solvent, the resulting slurry was pressed onto the nickel foam using a 10 MPa force to assemble the working electrodes, which were subsequently dried at 80 °C for 8 h. Each working electrode contained approximately 5 mg of activated carbon samples and had a geometric surface area of 1 $cm^2$.

An electrochemical workstation (CHI660D, China) was used to reveal the electrochemical properties of each electrode by applying a three-electrode system in 6 M KOH electrolyte. A platinum sheet electrode was selected as the counter electrode, while a saturated calomel electrode served as the reference electrode. Cyclic voltammetry (CV) measurements were performed over a potential range from −1.1 to −0.1 V at a scan rate of 5 mV $s^{-1}$. The cycle lifetimes of the electrodes were tested for 2000 cycles by galvanostatic charge–discharge (GCD) measurements over a potential range from −1.1 to −0.1 V and at a current density of 5 A $g^{-1}$. The specific capacitance of the corresponding electrodes at 1, 100, 250, 500, 750, 1000, 1250, 1500, 1750 and 2000 cycles were calculated by eqn (3), respectively:

$$C = (I \times t) \times (\Delta U \times m)^{-1} \quad (3)$$

where $C$ is specific capacitance, $I$ is discharging current, $\Delta U$ is the total change in voltage and $m$ is the mass of the active material in each electrode.

## 3. Results and discussion

### 3.1 XPS analysis

X-ray photoelectron spectroscopy (XPS) was used to investigate the chemistry of the carbon surface to identify and quantify the basic elements (except for hydrogen and helium) and the chemical functional groups. Table 1 shows the composition of the surface atomic elements and the chemical functional groups of LCA and LCANH. It can be concluded that the plasma treatment leads to an increase in the content of oxygen from 23.7% to 30.1%, showing oxygen incorporation on the LCANH surface. This result may be related to the reactions of hydroxyl and oxygen ions excited from the $NH_3 \cdot H_2O$ molecule with the LCA surface. This fact also may be attributed to the reactions of radicals generated by plasma treatment with oxygen from the atmosphere after the treated carbon sample was exposed to the air.[24] The relative nitrogen content increased from 0.1% to 2.4% after plasma treatment, implying a successful nitrogen incorporation. The spectra of C 1s, O 1s and N 1s were fitted into several Gaussian bands based on the previous literature, and the results are presented in Table 2 and Fig. 2.[25,26] It can be observed that the content of –C–C– dramatically decreased from 83.2% to 50.7% after plasma treatment, whereas an increase in the contents of –C–O, –C═O, and O–C═O can be observed. These results are attributed to the nitrogen and oxygen ion bombardment, which results in the rupture of –C–C– and the creation of active sites and free radicals. Meanwhile, $NH_3 \cdot H_2O$ molecules are excited by DBD plasma and broken up into a series of products with radical sites. These products subsequently interact with the free radicals at activated sites and non-activated sites in the carbon samples, leading to the successful incorporation of new functional groups (*e.g.* –C–O, –C═O and O–C═O). The spectra of N 1s show that various nitrogen-containing functional groups are incorporated on the LCANH surface after plasma treatment. Pietrzak found that the nitrogen

 

Table 1 Composition of surface atomic elements and chemical functional groups of LCA and LCANH

| | B.V. (eV) | Assignment | LCA | LCANH |
|---|---|---|---|---|
| **Components (%)** | | | | |
| *C 1s* | | | | |
| C1 | 284.8 | –C–C– or –C–H | 83.2 | 50.7 |
| C2 | 286.5 | –C–O or –C–N– | 11.5 | 30.9 |
| C3 | 288.0 | –C═O or O–C–O | 5.3 | 9.1 |
| C4 | 289.1 | O–C═O or –C═N or –N═C–O– | — | 9.3 |
| *N 1s* | | | | |
| N1 | 398.6 | Pyridinic (N6) | — | 24.7 |
| N2 | 399.7 | Imine, amines, amides | — | 35.3 |
| N3 | 400.3 | Pyrrolic and pyridonic (N5) | — | 32.8 |
| N4 | 401.2 | Nitrogen substituents in aromatic graphene structures–quaternary nitrogen (N–Q) | — | 7.2 |
| *O 1s* | | | | |
| O1 | 530.6 | –C═O | 40.5 | 45.2 |
| O2 | 532.2 | Carbonyl oxygen atoms in esters, amides, anhydrides and oxygen atoms in hydroxyls or ethers | 28.3 | 24.5 |
| O3 | 533.2 | Ether oxygen atoms in esters and anhydrides | 17.1 | 13.1 |
| O4 | 534.1 | Oxygen atoms in acidic carboxyl groups | 14.1 | 17.2 |
| **Atomic composition (%)** | | | | |
| C | | | 76.2 | 67.5 |
| O | | | 23.7 | 30.1 |
| N | | | 0.1 | 2.4 |

Table 2 Structural parameters of LCA and LCANH based on XRD patterns

| | 002 peak | | | | 101 peak | | | |
|---|---|---|---|---|---|---|---|---|
| Samples | $\beta$ | $2\theta(^\circ)$ | $d_{002}$ (nm) | $L_c$ (nm) | $\beta$ | $2\theta$ (°) | $d_{101}$ (nm) | $L_a$ (nm) |
| LCA | 11.474 | 24.66 | 0.360 | 0.708 | 4.790 | 43.82 | 0.206 | 3.653 |
| LCANH | 12.205 | 25.08 | 0.355 | 0.667 | 5.311 | 43.82 | 0.206 | 3.295 |

species of pyrrolic and pyridonic nitrogen (N-5, 400.3 eV) and *N*-pyridine oxide (*N*-oX, 402.5 eV) have the most positive effects on the electrochemical properties of the carbon material.[26] Moreover, Thorogood reported that the content of quinonyl (–C═O) has a positive correlation with the electrochemical properties of the carbon material.[27] In this study, both spectra of C 1s and O 1s demonstrated that plasma treatment leads to an increase in the content of –C═O. Furthermore, the spectrum of N 1s shows that the content of N-5 predominates (32.8%). Therefore, these facts may synergistically enhance the electrochemical properties of LCANH.

### 3.2 ESR analysis

The *g* factors and free radicals concentration of LCA and LCANH are presented in Fig. 3. It is well known that the ion bombardment in plasma treatment can lead to the rupture of initial chemical bonds in a material's surface, thereby generating large numbers of free radicals. These free radicals show high chemical activity, favouring cross-linking reactions. It can be concluded from Fig. 3 that the free radicals' concentration of LCANH is increased by 85.6% after plasma treatment and reaches 1.16 × 1018 spins $g^{-1}$. The dramatic decrease in the content of –C–C– described in the XPS analysis may be responsible for the formation of free radicals, which subsequently react with the plasma excited products, resulting in the formation of stable nitrogen-containing and oxygen-containing chemical bonds. The *g* factor value reveals information about the free radicals type; whereby a *g* factor value greater than 2.0040 is attributed to oxygen-centred radicals, while a *g* factor value less than 2.0030 corresponds to carbon-centred radicals. Moreover, a *g* factor value in the range of 2.0030–2.0040 represents mixed carbon-centred and oxygen-centred radicals.[28] It can be observed from Fig. 3, that the *g* factor is changed from 2.0038 to 2.0040 after plasma treatment, indicating the conversion of free radicals from a combination of carbon-centred and oxygen-centred radicals into oxygen-centred radicals. This fact is related to the formation of oxygen-containing groups on the carbon surface, as confirmed by XPS analysis.

### 3.3 Porous structure analysis

Fig. 4 shows the $N_2$ sorption isotherms and the BJH pore size distributions of LCA and LCANH. It can be observed that all the

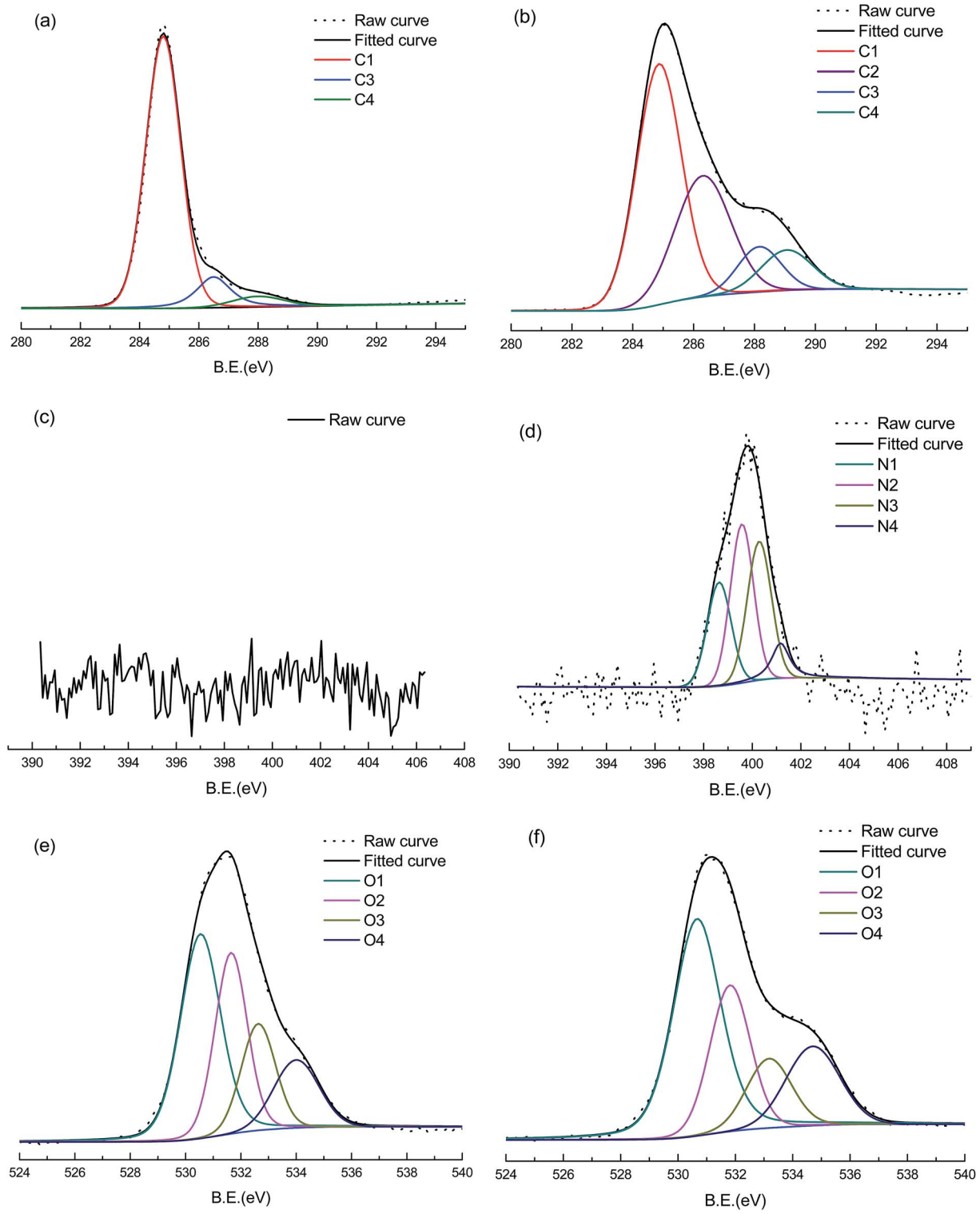


Fig. 2 High-resolution XPS of LCA and LCANH: (a), (b) deconvolution for C 1s spectra, (c), (d) deconvolution for N 1s spectra, (e), (f) deconvolution for O 1s spectra.

samples demonstrate type I isotherm curves based on the IUPAC classification.[29] A nearly vertical adsorption line appears at a relative pressure of less than 0.10, while a relatively horizontal adsorption plateau is observed at higher relative pressure. This indicates the presence of dominant micropores in the texture. However, the appearance of a slight deviation from a nearly horizontal plateau and hysteresis loop at a relative pressure range of 0.10–0.99 implies the existence of some

 

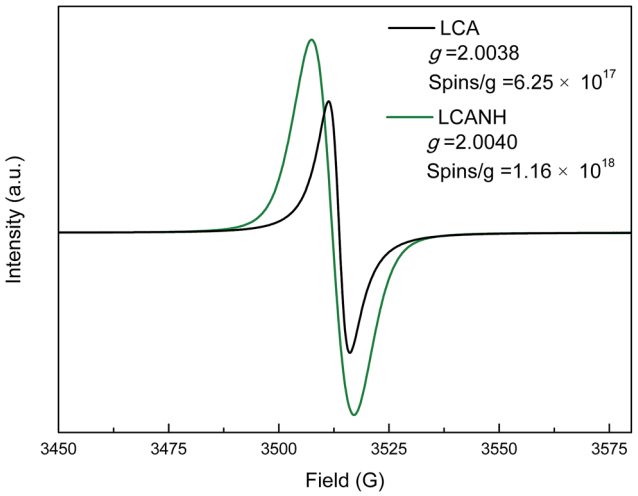


Fig. 3 ESR spectra of LCA and LCANH.

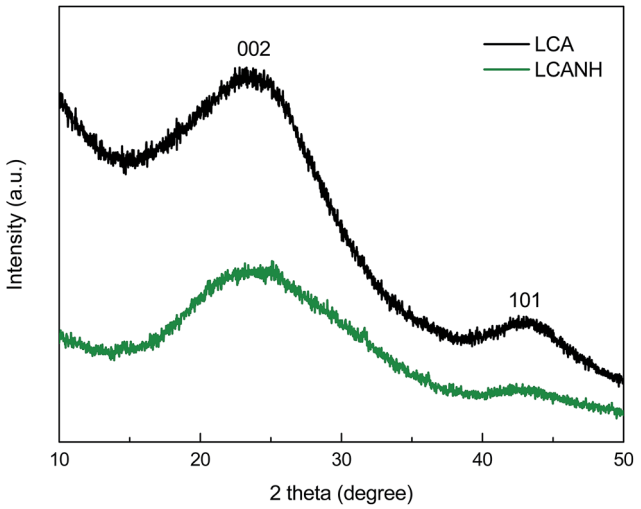


Fig. 5 XRD patterns of LCA and LCANH.

mesopores.[30] The BET surface area of LCANH is increased by 21.7% after plasma treatment and reaches 1822.9 $m^2 g^{-1}$, which may be attributed to the surface etching effect by DBD plasma on the carbon framework, resulting in the collapse of macropores and the opening of dead pores.[21] The proportion of micropores is increased from 78.5% to 85.2% after plasma treatment, which may be responsible for the increase in BET surface area. These improvements of the porous texture ensure a highly accessible surface area for the accumulation of electrolyte ions, which can enhance the electrochemical properties. The insert of Fig. 4 shows the pore distribution. It can be observed that most of the pore sizes in both LCA and LCANH are less than 3 nm, which confirms the high proportion of micropores in the texture.

### 3.4 XRD analysis

Fig. 5 presents the XRD patterns of LCA and LCANH. Two broad peaks at $2\theta$ values of approximately 25° and 43° can be observed, corresponding to the lattice planes of 002 and 101, respectively. Table 2 shows the parameters of the microcrystalline structure of LCA and LCANH, which were calculated using the Bragg equation and Scherrer's equation. LCANH demonstrates a higher $\beta$ in the 002 lattice plane in comparison to LCA, which indicates that plasma treatment leads to a more amorphous structure being formed. It has been proven that heteroatom incorporation preferably occurs in the amorphous regions and the graphite edges of the carbon structure, which can be reflected by the change in $d_{002}$, $L_c$ and $L_a$.[31] In addition,

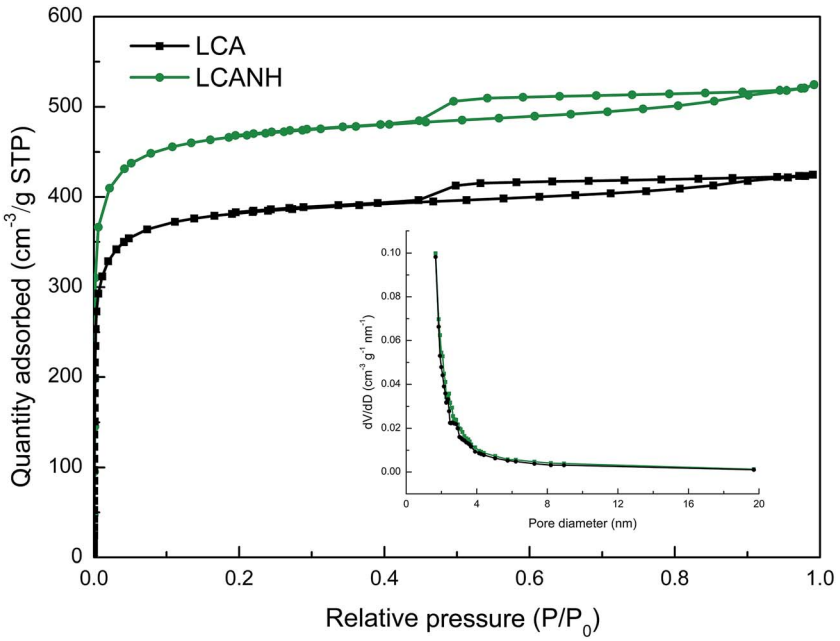


Fig. 4 N2 sorption isotherms of LCA and LCANH. Insert: BJH pore size distributions of LCA and LCANH.

a slightly decrease in $d_{002}$ and a significant decrease in $L_c$ and $L_a$ of LCANH were observed. This implied that the plasma treatment may create carbon defects in the LCANH structure, which may be responsible for the increase in specific surface area, as proven by BET analysis.

### 3.5 Raman analysis

However, the XRD technique alone is not sufficient to reveal the amorphous carbon structure. Raman spectroscopy was applied to reveal the aromatic and amorphous carbon structure due to its high sensitivity. The Raman spectra of LCA and LCANH are presented in Fig. 6. Both LCA and LCANH show the typical structure of $sp^2$ carbons containing two prominent first order peaks, which imply a structural disorder and multiphase in the carbon structure. A significant decrease in signal intensity of LCANH is observed. This may be related to the developed porosity after plasma treatment, which leads to the scattering and trapping of the incident laser and Raman signal.[21] The Raman spectra corresponding to the first order (800–1800 $cm^{-1}$) of all the carbon samples fitted into 4 Gaussian bands, which represent the typical aromatic or amorphous structure, as shown in Fig. 6. The band at 1586 $cm^{-1}$ (G) corresponds to the graphitic order. The band at 1332 $cm^{-1}$ (D) is attributed to the disorder in the carbon structure. The band at 1210 $cm^{-1}$ is related to the impurities in the graphite lattice. The band at 1480 $cm^{-1}$ reflects the stacking defects in the graphene layer. Table 3 shows the Raman parameters of LCA and LCANH. It can be observed that the wavenumber of the D band shifts from 1332 $cm^{-1}$ to 1334.5 $cm^{-1}$ and the FWHM of the D band is slightly increased after plasma treatment. These results are related to the incorporation of heteroatoms (oxygen and nitrogen) and the development of a porous texture. The $A_D/A_G$ of LCANH is slightly increased, which indicates that the graphitic order diminishes with plasma treatment. The surface incorporation of oxygen-containing and nitrogen-containing groups modifies the angles and bond lengths of the graphitic layers, diminishing the intensity of π–π interactions between themselves.[32] This result may be also attributed to the greater porous texture of LCANH. It should be noted that the development of porosity leads to the expansion of the defective graphitic structure.

### 3.6 Electrochemical properties

The electrochemical properties of the electrodes were investigated using cyclic voltammetry (CV) measurements in 6.0 M KOH electrolyte solution (potential range, −1.1 to −0.1 V; sweep rate, 5 mV $s^{-1}$), and the results are presented in the insert of Fig. 7. LCA exhibited a rectangular-like voltammogram, implying a highly reversibility and capacitance of this electrode. However, the CV curve of LCANH displayed a pair of redox peaks within the potential range from −0.3 to −0.8 V and showed a slight delay at potential reversal, indicating the presence of

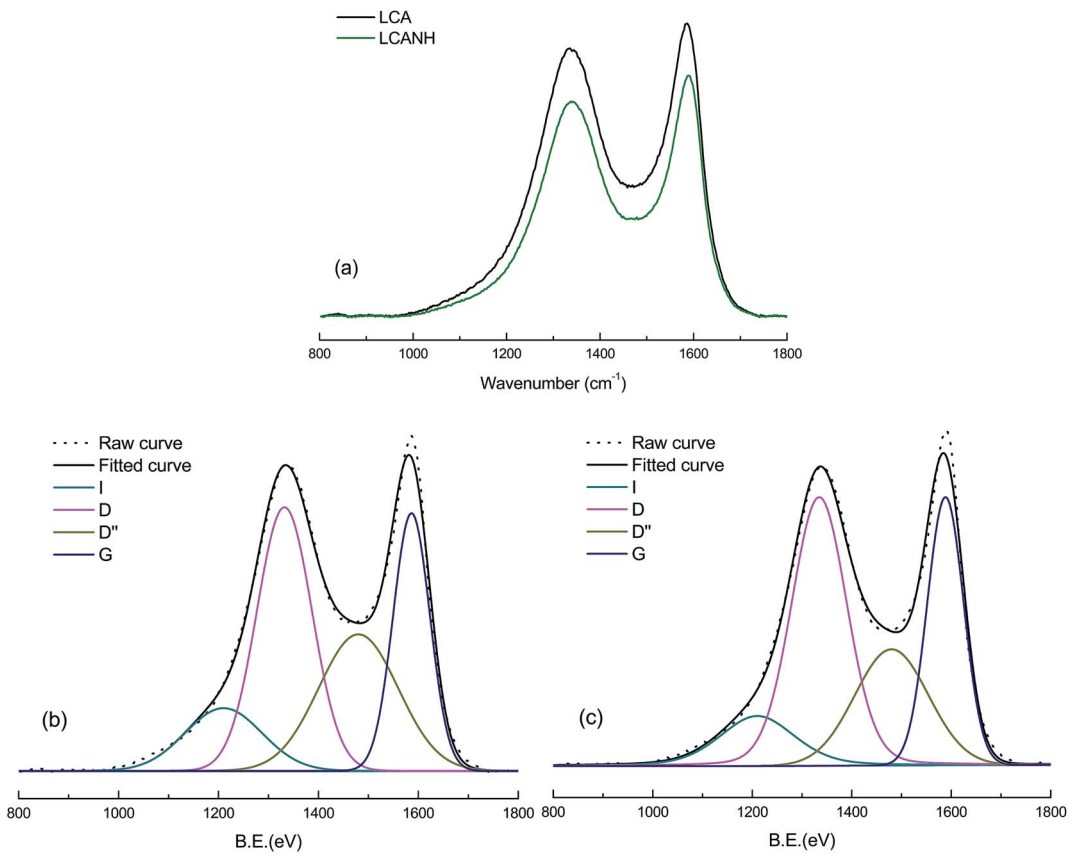


Fig. 6 Raman spectra of (a) signal intensity curves, (b) deconvolution for the curve of LCA (c) deconvolution for the curve of LCANH.

 

Table 3 Raman parameters of LCA and LCANH

| | Assignments | Parameter values | |
|---|---|---|---|
| | | LCA | LCANH |
| Bands ($cm^{-1}$) | | | |
| I | Impurities in the graphite lattice | 1210.0 | 1211.6 |
| D | Disorder in the LCA structure | 1332.0 | 1334.5 |
| D′ | Stacking defects in the graphene layer | 1480.2 | 1480.0 |
| G | Graphitic order | 1586.3 | 1586.2 |
| $FWHM_D$ | Full width at the half maximum of D-band peak | 129.96 | 131.01 |
| $A_D/A_G$ | Degree of disorder: area ratio of D-band to G-band | 1.54 | 1.61 |

pseudo-capacitance. Plasma treatment introduces oxygen-containing groups onto the carbon surface, which provide strong polar sites. Faradic reactions occur at these polar sites, leading to adsorbing water molecules, thus hindering the migration of electrolytes in the porous structure.[33] In addition, the presence of nitrogen-containing groups (*e.g.* amides, pyrrolic and pyridonic nitrogen) may also retard the motion of electrolytes, which resulted in an increase in ohmic resistance of the electrolytes along the axial direction of the carbon samples.[34] Generally, the integrated area of a CV curve is used for evaluating specific electrochemical capacitance. LCANH demonstrated an obvious increase in both the double-layer capacitance and pseudo-capacitance. It has been proved that fast faradic reactions take place at the carbonyl functional group (–C═O) of carbon samples, which leads to an enhanced accessibility to hydrophilic carbon coverage in an aqueous electrolyte.[33] In addition, the hydroquinone-type complex (*i.e.* $C_xOH$) between protons and quinone-type groups is formed when electrons transfer across the double-layer, which provides redox activity and may be related to the presence of a faradaic current.[35,36] XPS analysis proved that the contents of –C═O in the carbon samples after plasma treatment increased. This result may be responsible for the increase in pseudo-capacitance of LCANH. Moreover, nitrogen-containing groups with an electron-rich phenyl ring may also act as redox sites and participate in the redox reactions due to their electron-donating capability, thus promoting the pseudo-capacitance of the carbon electrodes.[36] In the other aspect, the improved porous texture in LCANH, as proved by BET analysis, may also be related to the enhancement of the electrochemical properties.

In order to reveal the cycling stability of the electrodes, galvanostatic charge–discharge (GCD) measurements were performed for 2000 cycles in 6 M KOH electrolyte solution at a current density of 5 A $g^{-1}$. The specific capacitances at the cycles of 1, 100, 250, 500, 750, 1000, 1250, 1500, 1750 and 2000 are given in Fig. 7. The highest specific capacitance at the first cycle calculated from the GCD curve was observed in LCANH and reached 271.7 F $g^{-1}$, which was 74.16% higher than that of

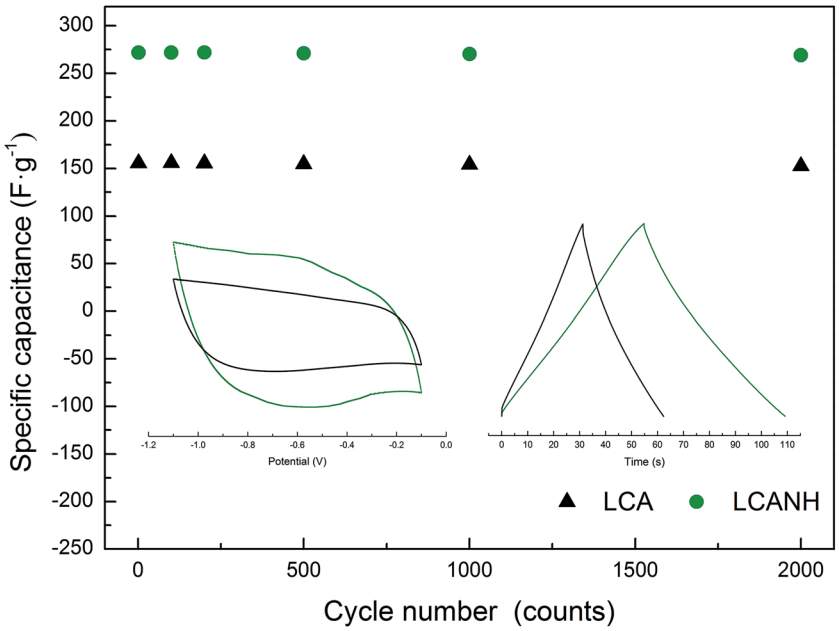


Fig. 7 Cycle stability of the electrodes using GCD measurement at a current density of 10 A $g^{-1}$ and in 6 M KOH aqueous electrolyte. Inset: left, CV curves of the electrodes over a potential range from −1.1 to −0.1 V at a sweep rate of 5 mV $s^{-1}$; right, GCD curves of the first cycle number.

LCA. No electrodes exhibited an obvious decay in specific capacitance. The electrode from LCANH retained 99.2% of the initial specific capacitance value after 2000 cycles, which was a slightly higher number than that of LCA. It can be concluded that both the specific capacitance and electrochemical reproducibility of the electrode from LCANH were enhanced.

## 4. Conclusions

$NH_3 \cdot H_2O$ DBD plasma treatment leads to positive synergistic effects on electrochemical properties of lignin-based activated carbon (LCA), demonstrating a highest specific capacitance of 271.7 F $g^{-1}$ for LCANH at a current density of 5 A $g^{-1}$, which was 74.2% higher in comparison to LCA. Large numbers of free radicals were generated during $NH_3 \cdot H_2O$ DBD plasma treatment and both nitrogen- and oxygen-containing groups, especially quinonyl (–C=O) and pyrrolic or pyridonic nitrogen (N-5), were successfully incorporated onto the carbon surface. Plasma treatment also led to an increase in both the specific surface area and micropores volumes of LCANH. These facts synergistically enhance the electrochemical properties.

## Acknowledgements

The authors are grateful for the support by projects from the Natural Science Foundation of Jiangsu Province (Grant No. BK20161524), the National Natural Science Foundation of China (Grant No. 31400515 and Grant No. 31270606), the Doctorate Fellows Foundation of Nanjing Forestry University, the Jiangsu Province Ordinary University Students' Scientific Research Innovation Project (Grant No. KYZZ16_0320), and the Priority Academic Program Development of Jiangsu Higher Education Institutions (PAPD). Also this paper was sponsored by Qing Lan Project.

## References

1 P. C. R. Pinto, C. Oliveria, C. A. Costa, A. Gaspar, T. Faria, J. Ataide and A. E. Rodrigues, *Ind. Crops Prod.*, 2015, **71**, 153.
2 C. Peng, X. B. Yan, R. T. Wang, J. W. Lang, Y. J. Ou and Q. J. Xue, *Electrochim. Acta*, 2013, **87**, 401.
3 K. Kuratani, K. Okuno, T. Lwaki, M. Kato, N. Takeichi, T. Miyuki, T. Awaza, M. Majima and T. Sakai, *J. Power Sources*, 2011, **196**, 10788.
4 Y. K. Lv, L. H. Gan, M. X. Liu, W. Xiong, Z. J. Xu, D. Z. Zhu and D. S. Wright, *J. Power Sources*, 2012, **209**, 152.
5 H. Zhang, G. P. Cao and Y. S. Yang, *Energy Environ. Sci.*, 2009, **2**, 932.
6 V. Barranco, M. A. Lillo-Rodenas, A. Linares-Solano, A. Oya, F. Pico, J. Ibanez, F. Agullo-Rueda, J. M. Amarilla and J. M. Rojo, *J. Phys. Chem. C*, 2010, **114**, 10302.
7 J. Yan, T. Wei, B. Shao, F. Q. Ma, Z. J. Fan, M. L. Zhang, C. Zheng, Y. C. Shang, W. Z. Qian and F. Wei, *Carbon*, 2010, **48**, 1731.
8 H. C. Huang, D. Q. Ye and B. C. Huang, *Surf. Coat. Technol.*, 2007, **201**, 9533.
9 C. L Chen, B. Liang, D. Lu, A. Ogino, X. K. Wang and M. Nagatsu, *Carbon*, 2010, **48**, 939.
10 E. Raymundo-Pinero, D. Cazorla-Amoros and A. Linares-Solano, *Carbon*, 2003, **41**, 1925.
11 M. C. Huang and H. S. Teng, *Carbon*, 2003, **41**, 951.
12 M. G. Plaza, C. Pevida, A. Arenillas and F. Rubiera, *Fuel*, 2007, **86**, 2204.
13 R. Pietrzak, K. Jurewicz, P. Nowicki, K. Babel and H. Wachowska, *Fuel*, 2007, **86**, 1086.
14 K. Jurewicz, K. Babel, A. Ziolkowski and H. Wachowska, *Electrochim. Acta*, 2003, **48**, 1491.
15 R. Pietrzak, H. Wachowska and P. Nowicki, *Energy Fuels*, 2006, **20**, 1275.
16 K. Jurewicz, K. Babel, A. Ziolkowski, H. Wachowska and M. Kozlowski, *Fuel Process. Technol.*, 2002, **77**, 191.
17 G. Lota, J. Tyczkowski, R. Kapica, K. Lota and E. Frackowiak, *J. Power Sources*, 2010, **195**, 7535.
18 J. Y. Zhou, Z. W. Wang, R. Zuo, Y. Zhou, X. M. Cao and K. Cheng, *Asia-Pac. J. Chem. Eng.*, 2012, **7**, 245.
19 N. Inagaki, K. Narushima, H. Hashimoto and K. Tamura, *Carbon*, 2007, **45**, 797.
20 D. Lee, S. H. Hong, K. H. Paek and W. T. Ju, *Surf. Coat. Technol.*, 2005, **200**, 2277.
21 R. K. Gupta, M. Dubey, P. Kharel, Z. R. Gu and Q. H. Fan, *J. Power Sources*, 2015, **274**, 1300.
22 Y. C. Xu, M. Z. Chen and X. Y. Zhou, *BioResources*, 2017, **12**, 1403.
23 J. Zhang, L. X. Yu, Z. C. Wang, Y. M. Tian, Y. N. Qu, Y. Wang, J. J. Li and H. Q. Liu, *J. Chem. Technol. Biotechnol.*, 2011, **86**, 1177.
24 N. K. Agrawal, R. Agarwal, A. K. Gautam, Y. K. Vijay and K. C. Swami, *Mater. Sci.*, 2015, **51**, 68.
25 A. Alabadi, S. Razzaque, Y. W. Yang, S. Chen and B. Tan, *Chem. Eng. J.*, 2015, **281**, 606.
26 R. Pietrzak, *Fuel*, 2009, **88**, 1871.
27 C. A. Thorogood, G. G. Wildgoose, J. H. Jones and R. G. Compton, *New J. Chem.*, 2007, **31**, 958.
28 V. C. Di, K. M. Neyman, T. Risse, M. Sterrer, E. Fischbach, H. J. Freund, V. A. Nasluzov, G. Pacchioni and N. Rosch, *J. Chem. Phys.*, 2006, **124**, 044708.
29 K. S. W. Sing, D. H. Everett, R. A. W. Haul, L. Moscou, R. A. Pierotti, J. Rouquerol and T. Siemieniewska, *Pure Appl. Chem.*, 1985, **57**, 603.
30 Y. A. Hamed and H. S. Bamufleh, *Fuel*, 2009, **88**, 87.
31 H. M. Lee, H. G. Kim, S. J. Kang, S. J. Park, K. H. An and B. J. Kim, *J. Ind. Eng. Chem.*, 2015, **21**, 736.
32 S. Zhang, Z. H. Min, H. L. Tay, M. Asadullah and C. Z. Li, *Fuel*, 2011, **90**, 1529.
33 C. T. Hsieh and H. Teng, *Carbon*, 2002, **40**, 667.
34 C. T. Hsieh, H. Teng, W. Y. Chen and Y. S. Chen, *Carbon*, 2010, **48**, 4219.
35 M. Miranada-Hernandez and M. E. Rincon, *J. Solid State Electrochem.*, 2005, **9**, 646.
36 A. Felten, C. Bittencourt, J. J. Pireaux, G. Van Lier and J. C. Charlier, *J. Appl. Phys.*, 2005, **98**.

 